Supplementary Information

Pentavalent Ta-Substitution Enhances Ionic Conductivity and Critical Current Density in NASICON for Sodium-Ion Batteries

Vishal Ranawade[a,b], Deepak Kumar Gorai[a,c], M. Dinachandra Singh[a], Xiang You[b], Ajay Shinde[a], Kanwar S Nalwa[a], Raju Kumar Gupta[a, d-g]*, Lingzi Sang[b]*, and Sudarshan Narayanan[a,e]*

[a]Department of Sustainable Energy Engineering, [c]Department of Materials Science and Engineering, [d]Department of Chemical Engineering, [e]Chandrakanta Kesavan Centre for Energy Policy and Climate Solutions, [f]Kotak School of Sustainability, [g]Center for Environmental Science and Engineering, Indian Institute of Technology Kanpur, Kanpur, 208016, India

[b]Department of Chemistry, University of Alberta, Edmonton, AB, T6G 2G2 Canada

*Corresponding author email: guptark@iitk.ac.in, lsang@ualberta.ca, and sudarshan@iitk.ac.in

Table of Contents

Figure S4 Total energy vs. Energy cutoff for the undoped $NZSP_{0.4}$.

Figure S5. Rietveld refinement plots of (a) $NZSP_{2.4}$ and (b) 8Ta-$NZSP_{2.4}$

Figure S6. Grain size distribution calculated from SEM images for (a) NZSP and (b) 8Ta-NZSP

Figure S7a. Elemental distribution mapping for pristine NZSP sample. (a) SEM image, (b) percentage distribution and (c) sum mapping spectra

Figure S7b. Elemental distribution mapping for pristine 8Ta-$NZSP_{0.4}$ sample. (a) SEM image, (b) percentage distribution and (c) sum mapping spectra

Figure S8. Density variation of xTa-$NZSP_{2.4}$ solid electrolyte after sintering.

Figure S9. Electrochemical equivalent circuit for EIS fitting

Figure S10. *DC polarization technique with a bias voltage of 0.1V, for* $NZSP_{2.4}$ *and 8Ta-*$NZSP_{2.4}$ *electrolyte*

Figure S11. *(a)* Na^+ *conduction mechanism in monoclinic structure; (b) Geometric illustration of the relaxed monoclinic crystal structure of* $NZSP_{2.4}$ *and Ta-substituted* $NZSP_{2.4}$

Figure S12. *The density of states of Monoclinic (a)* $NZSP_{2.4}$ *and (b) Ta-substituted* $NZSP_{2.4}$*.*

Figure S13. *NEB profiles for Monoclinic structure (a)* $NZSP_{2.4}$ *and (b) Ta-substituted* $NZSP_{2.4}$

Figure S14. *Theoretical properties comparison of C2-c and R3-c structure for* $NZSP_{2.4}$ *and Ta-substituted* $NZSP_{2.4}$

$Na_3V_2(PO_4)_3$ *Cathode Fabrication*

$Na_3V_2(PO_4)_3$ (NVP) was synthesized via a sol-gel method. Stoichiometric amounts of V_2O_5, $NH_4H_2PO_4$, and Na_2CO_3 in a molar ratio of 1:3:1.5, along with citric acid ($H_2C_2O_4$), were sequentially dissolved in 50 mL of deionized water at 80 °C under continuous stirring. The resulting solution was dried under vacuum conditions and pre-calcined at 350 °C for 2 hours in a tube furnace under an argon atmosphere. The resulting intermediate product was further calcined at 850 °C for 6 hours under argon to obtain the final NVP powder, which was then ground into a fine powder.

For cathode fabrication, a slurry was prepared by mixing the NVP powder, polyvinylidene fluoride (PVDF) binder, and acetylene black in a weight ratio of 7:1.5:1.5 using N-methyl-2-pyrrolidone (NMP) as the solvent. The mixture was homogenized using a Thinky centrifugal mixer and coated onto battery-grade aluminium foil with an automatic blade coater. The coated electrodes were dried in a vacuum oven at 120 °C for 24 hours. The dried cathodes were then compressed at 80 °C using a twin-roller calendaring machine. The final electrode, punched into discs of 10 mm diameter, exhibited a thickness of 42 μm and an active material loading of 3.03 mg cm^{-2}.

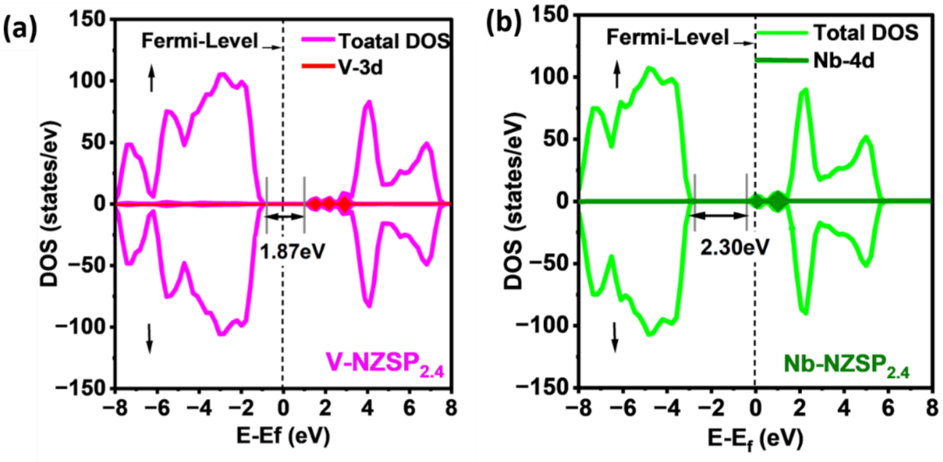

Figure S1. Bandgap calculations of rhombohedral V-$NZSP_{2.4}$ and Nb-$NZSP_{2.4}$

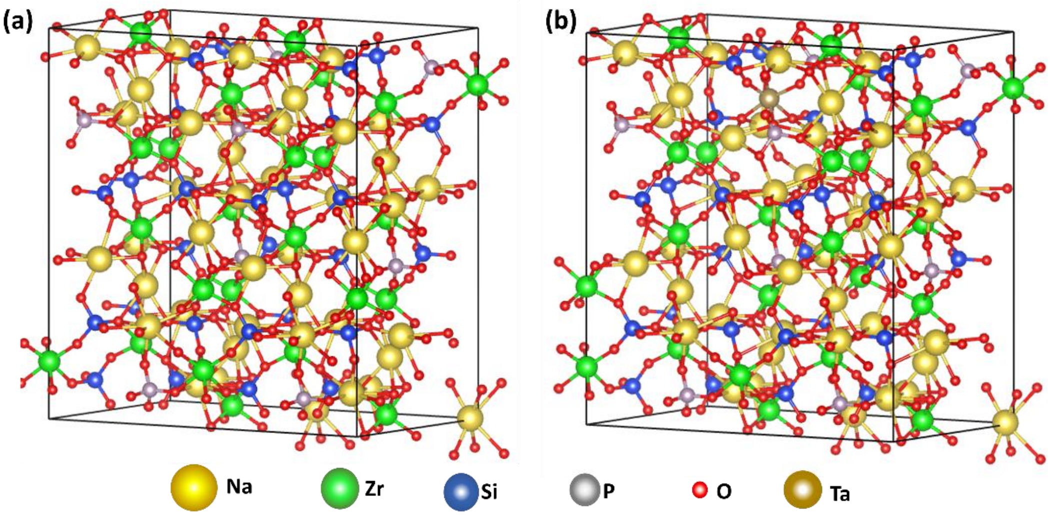

Figure S2. *Rhombohedral (R3c) supercell: (a) pristine NZSP composition,* Na_{41} Zr_{24} Si_{28} P_8 O_{144}, *(b) Ta-substituted NZSP,* Na_{40} $Zr_{23}Ta_1$ Si_{28} P_8 O_{144}.

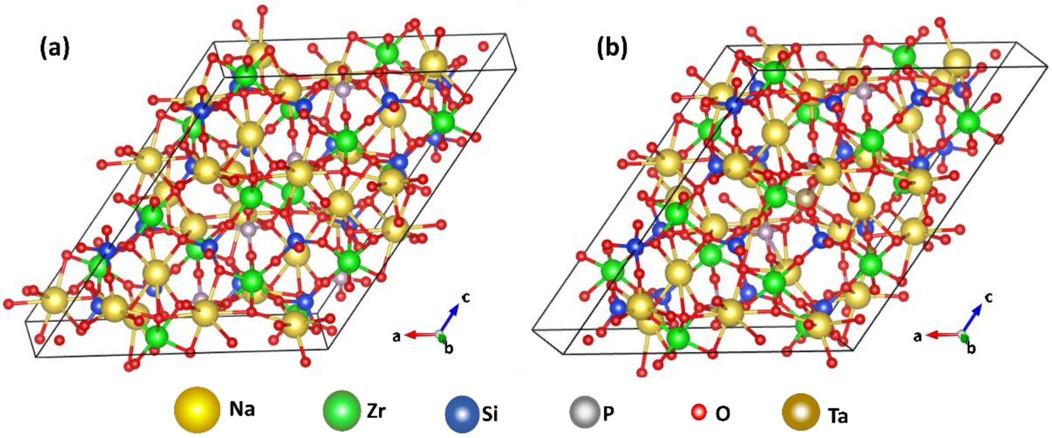

Figure S3. *Monoclinic (C2/c) supercell: (a) pristine NZSP,* $Na_{27}\ Zr_{16}\ Si_{19}\ P_5\ O_{96}$. *Ta-substituted NZSP,* $Na_{26}\ Zr_{15}Ta_1\ Si_{19}\ P_5\ O_{96}$.

For the rhombohedral NZSP (R3c) phase, we used a $1 \times 2 \times 1$supercell (245 atoms; $Na_{41}\ Zr_{24}\ Si_{28}\ P_8\ O_{144}$), which close to the $NZSP_{2.4}$ composition. In the main text, we referred to the 123-atom crystallographic cell ($Z = 6$) for clarity. The structure is shown in **Fig. S2(a)**. Increasing the cell size further (>250 atoms) significantly increases computational cost for DFT calculations, and the current calculated results remain consistent with experiment and literature. For the monoclinic NZSP (C2/c) phase, we constructed a $1 \times 1 \times 2$ supercell (163 atoms; $Na_{27}\ Zr_{16}\ Si_{19}\ P_5\ O_{96}$), also closely matching $NZSP_{2.4}$. The model is provided in **Fig. S3(a).**

Initial structures for both phases were taken from the Materials Project (R3c: mp-2714434; C2/c: mp-2713548). The compositions presented in **Fig. S2(a)** and **Fig. S3(a)**, as well as assign the Ta position in the pristine $NZSP_{2.4}$, we used the Minima Hopping Algorithm (MHA). Among the various configurations generated by MHA, the one with the lowest energy was used for further calculations of Ta-substituted $NZSP_{2.4}$. The Ta-doped models (rhombohedral $Na_{40}\ Zr_{23}\ Ta_1\ Si_{28}\ P_8\ O_{144}$; monoclinic $Na_{26}\ Zr_{15}\ Ta_1\ Si_{19}\ P_5\ O_{96}$) are shown in **Fig. S2(b)** and **Fig. S3(b)**. All structures were fully optimized using the parameters described in the Methods section 2.3, and NEB calculations were performed on the optimized supercells.

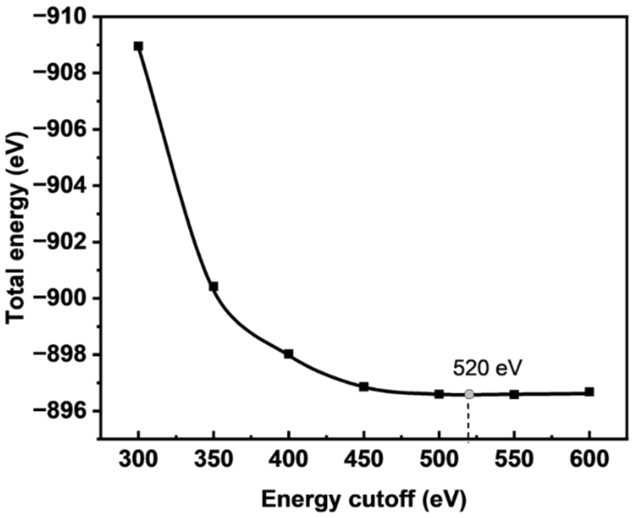

Figure S4. Total energy vs. Energy cutoff for the undoped $NZSP_{2.4}$.

An energy cutoff of 520 eV was employed for the plane-wave basis set, following prior literature reports [1–3]. This value was further validated for the undoped $NZSP_{2.4}$ system, and as demonstrated in **Fig. S4**, it ensures sufficient convergence of the DFT total energy calculations.

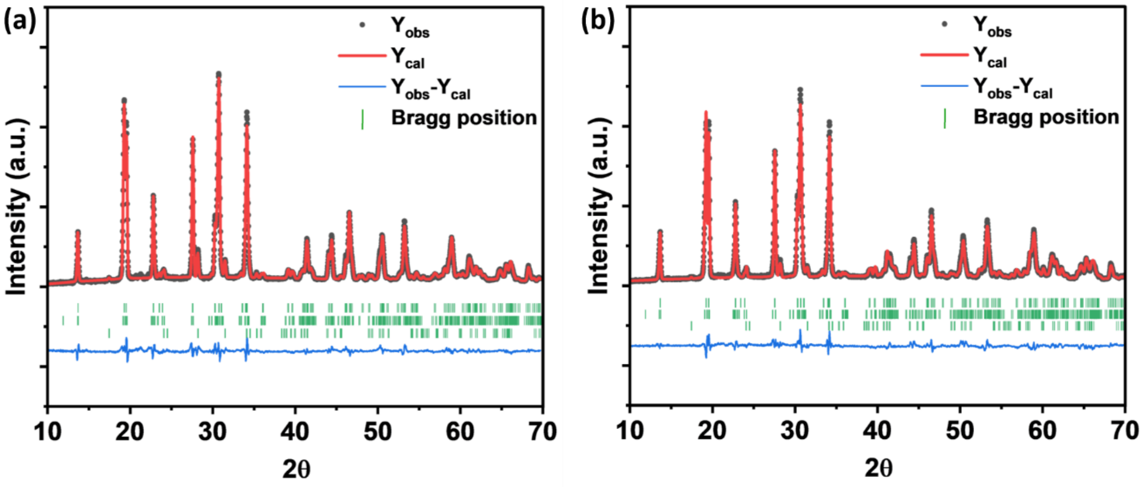

Figure S5. Rietveld refinement plots of (a) $NZSP_{2.4}$ and (b) 8Ta-$NZSP_{2.4}$.

Rietveld refinements were performed using the FullProf software. **Fig. S5** displays the multiphase profile refinements of (a) $NZSP_{2.4}$ (R_p = 9.52%, R_{wp} = 10.56%, and χ^2 = 1.477) and (b) 8Ta-$NZSP_{0.4}$ (Rp = 9.04%, R_{wp} = 10.08%, and χ^2 = 1.347), based on room-temperature PXRD data. The analysed solid electrolyte comprises $Na_{3.4}Zr_2Si_{2.4}P_{0.6}O_{12}$, R3-c (ICSD: 62386); C2-c (ICSD: 01-070-0234); and ZrO_2 (COD: 1010912).

Table S1. Structural parameters from Rietveld refinement of XRD data for pristine $NZSP_{2.4}$.

Phase fractions: C2/c NZSP2.4 (20.25%), R3c NZSP2.4 (76.25%), and ZrO_2 (3.50%)

(a)C2/c $NZSP_{2.4}$ phase:

a = 15.6672 Å, *b* = 9.0925 Å, *c* = 9.1792 Å, and *β* = 123.891°, *V* = 1085.469Å^3

Site	Wyckoff	*x*	*y*	*z*	*Occ*
Na1	4d	0.2500	0.2500	0.5000	0.881
Na2	4e	0.5000	0.889	0.2500	0.922
Na3	8f	0.7484	0.1641	0.6985	0.795
Zr1	8f	0.09905	0.2591	0.05231	0.9910
Si1	4e	0.0000	0.04124	0.2500	0.8000
Si2	8f	0.35817	0.0951	0.23278	0.805
P1	4e	0.0000	0.04124	0.2500	0.200
P2	8f	0.3581	0.09510	0.2327	0.195
O1	8f	0.29264	0.37002	0.4358	1.0000
O2	8f	0.47066	0.39667	0.10876	1.0000
O3	8f	0.2088	0.14909	0.28869	1.0000
O4	8f	0.4322	0.06314	0.16248	1.0000
O5	8f	0.50618	0.19311	0.54952	1.0000
O6	8f	0.10546	0.11478	0.31254	1.0000

(b) R3c $NZSP_{2.4}$ phase:

a = 9.101 Å, *b* = 9.101 Å, *c* = 22.685 Å, and *γ* = 120°, *V* = 1627.292 Å^3

Site	Wyckoff	*x*	*y*	*z*	*Occ*
Na1	6b	0.0000	0.0000	0.0000	0.421
Na2	18e	0.6297	0.03642	0.2600	0.620
Na3	36f	0.9539	0.8086	1.000	0.187
Zr1	12c	0.0000	0.0000	0.147	0.9750
Si1	18e	0.2998	0.01398	0.2606	0.7998
P1	18e	0.2998	0.01398	0.2606	0.2018
O1	36f	0.1992	0.0317	0.1922	1.000
O2	36f	0.2191	0.17274	0.06831	1.000

Table S2. Structural parameters from Rietveld refinement of XRD data for pristine 8Ta-NZSP$_{2.4}$.

Phase fractions: C2/c NZSP2.4 (22.30%), R3c NZSP2.4 (75.08%), and ZrO$_2$ (2.62%)

(a) C2/c NZSP$_{2.4}$ phase:

a = 15.670 Å, b = 9.088 Å, c = 9.1897 Å, and β = 123.519°, V = 1091.322Å^3

Site	Wyckoff	*x*	*y*	*z*	*Occ*
Na1	4d	0.2500	0.2500	0.5000	0.726
Na2	4e	0.5000	0.8787	0.2500	0.598
Na3	8f	0.7518	0.142	0.6761	1.000
Zr/Ta	8f	0.10346	0.25116	0.05326	0.95/0.05
Si1	4e	0.0000	0.03834	0.2500	0.800
Si2	8f	0.37067	0.0888	0.2263	0.800
P1	4e	0.0000	0.03834	0.2500	0.200
P2	8f	0.3581	0.09510	0.2327	0.200
O1	8f	0.16093	0.40349	0.1582	1.0000
O2	8f	0.47066	0.39667	0.10876	1.0000
O3	8f	0.20346	0.12799	0.24168	1.0000
O4	8f	0.4328	0.06314	0.16248	1.0000
O5	8f	0.4816	0.20425	0.44658	1.0000
O6	8f	0.08575	0.10416	0.31527	1.0000

(b) R3c NZSP$_{2.4}$ phase:

a = 9.0924 Å, b = 9. 0924 Å, c = 22.7965 Å, and γ = 120°, V = 1632.167 Å^3

Site	Wyckoff	*x*	*y*	*z*	*Occ*
Na1	6b	0.0000	0.0000	0.0000	0.34537
Na2	18e	0.6320	0.04756	0.2229	0.5324
Na3	36f	0.9492	0.82426	1.000	0.2419
Zr/Ta	12c	0.0000	0.0000	0.14836	0.95/0.05
Si1	18e	0.29152	0.00315	0.25613	0.8107
P1	18e	0.29152	0.00315	0.25613	0.1900
O1	36f	0.1953	0.03230	0.1899	1.000
O2	36f	0.2369	0.1867	0.05095	1.000

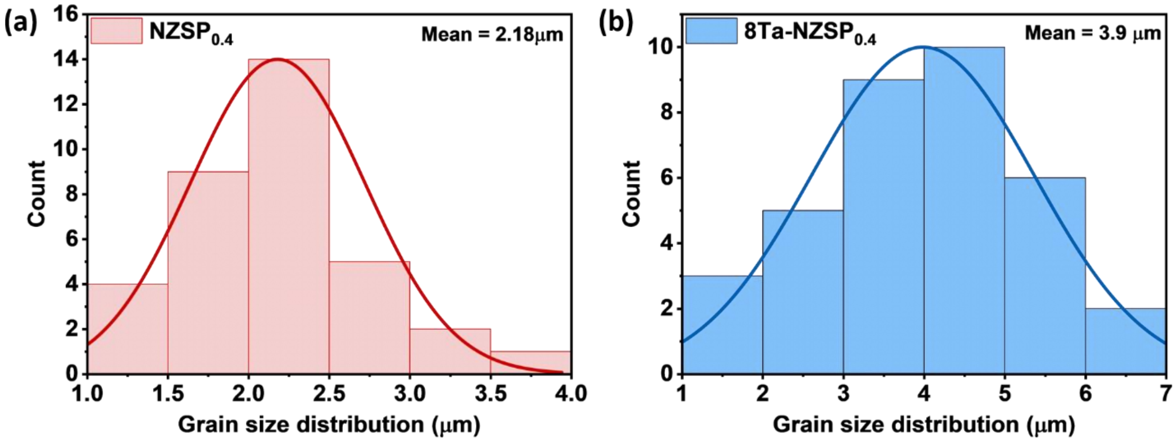

Figure S6. Grain size distribution calculated from SEM images for (a) NZSP$_{2.4}$ and (b) 8Ta-NZSP$_{2.4}$.

The grain size was determined using ImageJ software. SEM images of NZSP$_{2.4}$ and Ta-NZSP$_{2.4}$, shown in **Fig. 3(b)** and **Fig. 3(d)**, respectively, reveal that the undoped sample exhibits smaller grains with noticeable voids. In contrast, the Ta-doped sample displays larger grains with a more fused grain structure. As presented in **Fig. S6(a)**, the undoped sample shows a mean grain size of 2.18 μm, while **Fig. S6(b)** indicates a mean grain size of 3.9 μm for the Ta-doped sample. These results are consistent with the morphological observations.

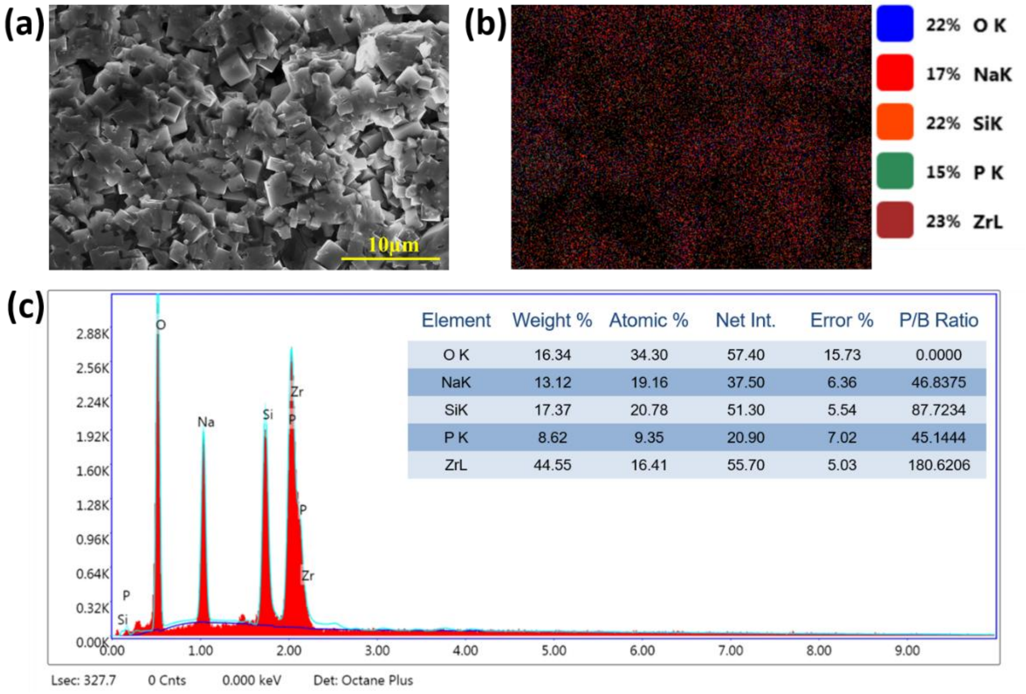

Element	Weight %	Atomic %	Net Int.	Error %	P/B Ratio
O K	16.34	34.30	57.40	15.73	0.0000
NaK	13.12	19.16	37.50	6.36	46.8375
SiK	17.37	20.78	51.30	5.54	87.7234
P K	8.62	9.35	20.90	7.02	45.1444
ZrL	44.55	16.41	55.70	5.03	180.6206

Figure S7a. Elemental distribution mapping for pristine NZSP sample. (a) SEM image, (b) percentage distribution and (c) sum mapping spectra.

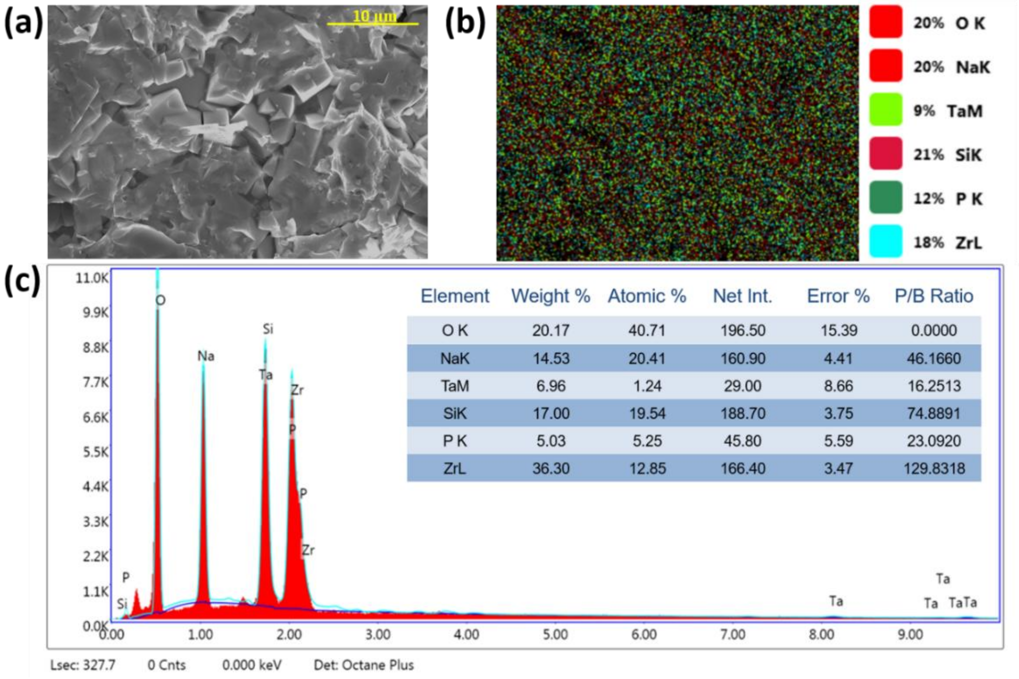

Element	Weight %	Atomic %	Net Int.	Error %	P/B Ratio
O K	20.17	40.71	196.50	15.39	0.0000
NaK	14.53	20.41	160.90	4.41	46.1660
TaM	6.96	1.24	29.00	8.66	16.2513
SiK	17.00	19.54	188.70	3.75	74.8891
P K	5.03	5.25	45.80	5.59	23.0920
ZrL	36.30	12.85	166.40	3.47	129.8318

Figure S7b. Elemental distribution mapping for pristine 8Ta-NZSP$_{0.4}$ sample. (a) SEM image, (b) percentage distribution and (c) sum mapping spectra.

EDS mapping of the Ta-NZSP$_{2.4}$ sample (**Fig. S7b**) reveals a lower atomic percentage of Zr compared to the pristine sample (**Fig. S7a**), along with an increased Ta content, suggesting that Ta partially substitutes Zr by approximately 8–9 at%. Additionally, the Ta-substituted sample exhibits a higher Si/P atomic ratio compared to the unsubstituted counterpart. While the elemental quantification may include some errors, as indicated in **Fig. S7a(c)** and **Fig. S7b(c)**, the results still provide a reasonable estimation of the elemental distribution. Notably, both the unsubstituted and Ta-substituted samples show elemental compositions that are tentatively consistent with the intended chemical formula.

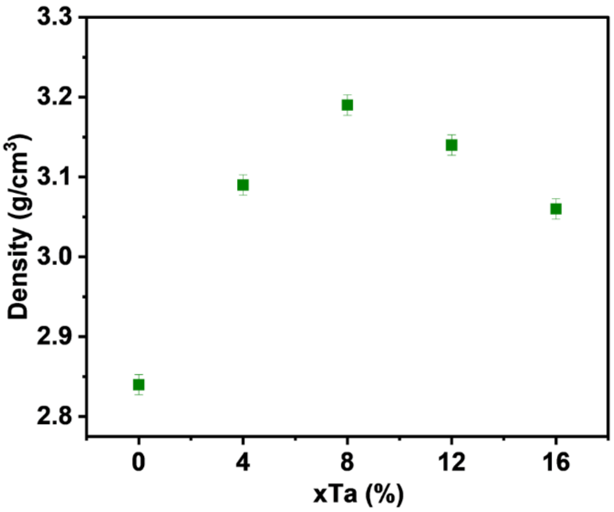

Figure S8. Density variation of xTa-NZSP$_{2.4}$ solid electrolytes after sintering.

The densities, determined by a conventional weighing technique, were 2.84±0.01 g/cm^3 for NZSP$_{2.4}$ and 3.19±0.01 g/cm^3 for 8Ta-NZSP$_{2.4}$. The density variation of NZSP$_{2.4}$ and Ta-doped NZSP after sintering depicted in the **Fig. S8**.

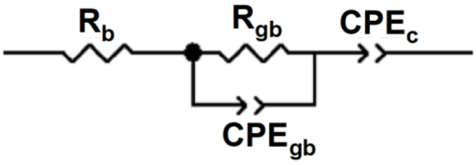

Figure S9. Electrochemical equivalent circuit for EIS fitting.

The EIS plots were analysed by fitting them to the electrochemical equivalent circuit depicted in **Fig. S9**. The grain resistance (R_b) dominates at higher frequencies (>10^4 Hz), and the grain boundary resistance (R_{gb}), along with its constant phase element (CPE_{gb}), appears in the midfrequency range (10^2–10^4 Hz). At lower frequencies ($<10^2$ Hz), the constant phase element for diffusion (CPE_c) emerges, indicating the impact of ionic diffusion in the system. Total ionic conductivity (σ_t) was determined using the equation:

$$\sigma_t = \frac{t}{(R_b + R_{gb})\pi(\frac{d}{2})^2}$$

Where *t* and *d* represent the thickness and diameter of the solid electrolyte pellet, respectively.

To measure the ionic transference number of the electrolyte, DC polarization technique was used. The ionic transference number (t_i) was calculated using the following formula:

$$t_i = \frac{I_t - I_e}{I_t}$$

where I_t represents the total current (the sum of ionic and electronic currents), and I_e is the electronic current of the electrolyte, which was approximately equal to the saturation current observed in a fully polarized electrolyte.

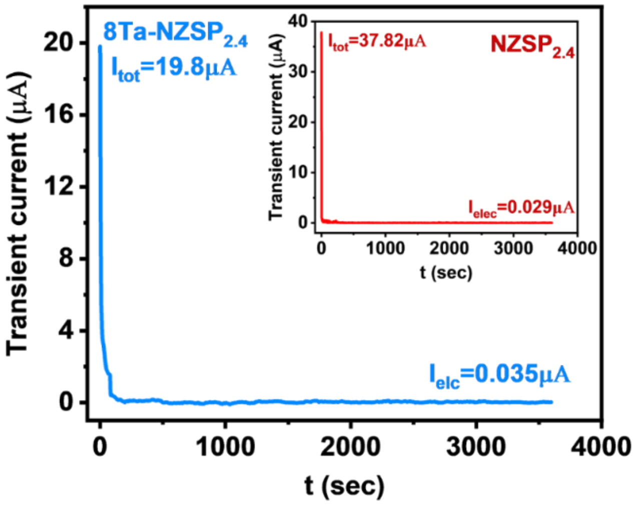

Figure S10. DC polarization technique with a bias voltage of 0.1V, for $NZSP_{2.4}$ and 8Ta-$NZSP_{2.4}$ electrolyte.

Fig. S10 shows the DC polarization for undoped and Ta-doped $NZSP_{2.4}$ at room temperature, where the ionic transference number for 8Ta-doped $NZSP_{2.4}$ was 0.9982, while for $NZSP_{2.4}$ it is 0.9992. These results indicate both Ta-doped and undoped samples have ionic transference numbers close to one, indicating that both electrolytes exhibit negligible electronic conductivity.

Table S3: Comparison of Electrochemical Performance with Literature

No.	**Material**	**Method of synthesis**	**Ionic Conductivity**	**Critical current density**	**Ref.**
1.	$Na_3Zr_2Si_2PO_{12}$ (NZSP)	SA-SSR*	0.67×10^{-3} S cm^{-1}	0.3 mA cm^{-2}	4
2.	$Na_{3.4}Zr_2Si_{2.4}P_{0.6}O_{12}$	SA-SSR*	5×10^{-3} S cm^{-1}	----	5
3.	NZSP-0.075Fe (Fe-NZSP)	SSR	0.423×10^{-3} S cm^{-1}	0.65 mA cm^{-2}	6
4.	$Na_{3.1}Zr_{1.95}Mg_{0.05}Si_2PO_{12}$ (Mg-NZSP$_{2.2}$)	SSR	3.2×10^{-3} S cm^{-1}	0.1 mA cm^{-2}	7
5.	$Na_{3.1}Y_{0.1}Zr_{1.9}Si_2PO_{12}$ (Y-NZSP)	SSR	1.21×10^{-3} S cm^{-1}	0.15 mA cm^{-2}	8
6.	$Na_{3.3}Zr_{1.9}Nb_{0.1}Si_{2.4}P_{0.6}O_{12}$(Nb-NZSP$_{2.4}$)	SA-SSR*	5.51×10^{-3} S cm^{-1}	0.05 mA cm^{-2}	9
7.	$Na_{3.2}Zr_{1.9}Sn_{0.1}Si_{2.2}P_{0.8}O_{12}$ (Sn-NZSP$_{2.2}$)	SSR	0.67×10^{-3} S cm^{-1}	0.3 mA cm^{-2}	10
8.	$Na_{3.3}Zr_{1.7}Pr_{0.3}Si_2PO_{12}$ (Pr-NZSP)	SSR	1.27×10^{-3} S cm^{-1}	0.9 mA cm^{-2}	11
9.	$Na_{3.3}Zr_{1.7}Eu_{0.3}Si_2PO_{12}$ (Eu-NZSP)	SSR	1.08×10^{-3} S cm^{-1}	0.6 mA cm^{-2}	11
10.	$Na_{3.3}Zr_{1.7}Lu_{0.3}Si_2PO_{12}$ (Lu-NZSP)	SSR	0.831×10^{-3} S cm^{-1}	0.45 mA cm^{-2}	11
11.	$Na_{3.1}Zr_{1.9}La_{0.1}Si_2PO_{12}$ (La-NZSP)	SA-SSR*	1.1×10^{-3} S cm^{-1}	0.6 mA cm^{-2}	12
12.	$Na_{3.1}Zr_{1.9}Sb_{0.1}Si_2PO_{12}$ (Sb-NZSP)	SSR	0.83×10^{-3} S cm^{-1}	0.4 mA cm^{-2}	13
13.	$Na_{3.4}Zr_{1.8}Ni_{0.2}Si_2PO_{12}$ (Ni-NZSP)	SSR	2.28×10^{-3} S cm^{-1}	0.9 mA cm^{-2} (30°C)	14
14.	$Na_{3.4}Zr_{1.7}Mn_{0.3}Si_2PO_{12}$ (Mn-NZSP)	SSR	1.58×10^{-3} S cm^{-1}	0.6 mA cm^{-2} (30°C)	14
15.	$Na_{3.2+2x}Zr_{1.8-x}Sc_{0.2}Zn_xSi_2PO_{12}$ (Sc-Zn-NZSP)	SSR	2.41×10^{-3} S cm^{-1}	0.9 mA cm^{-2}	15
16.	$Na_{3.4}Zr_{1.8}Cu_{0.2}Si_2PO_{12}$ (Cu-NZSP)	SSR	1.94×10^{-3} S cm^{-1}	0.5 mA cm^{-2}	16
17.	0.05k-NZSP (IM**)	SA-SSR*	0.67×10^{-3} S cm^{-1}	1.3 mA cm^{-2}	17
18	NZSP (SO***)	SSR	1.1×10^{-3} S cm^{-1}	0.95 mA cm^{-2}	18
19.	Ta-NZSP$_{2.4}$	SSR	4.34×10^{-3} S cm^{-1}	1.3 mA cm^{-2}	*This study

Note- We focus exclusively on performance improvements achieved via cation substitution in NZSP, and therefore exclude studies involving interface modification, grain-boundary engineering, elevated testing temperatures, or external stack pressures, as these approaches fall outside the scope of our work; IM**: Interface modification; SA-SSR*: Solution-assisted solid-state route, which typically delivers better performance than the conventional SSR (solid-state route), SO***: solid electrolyte synthesis process optimization

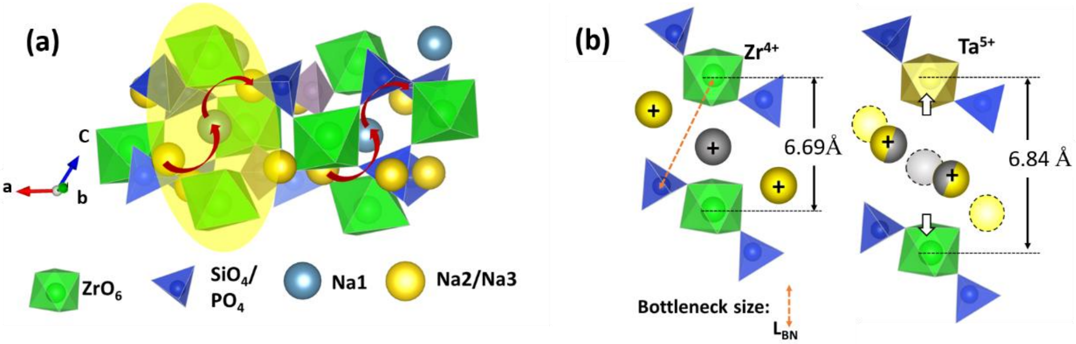

Figure S11. *(a) Na^+ conduction mechanism in monoclinic structure; (b) Geometric illustration of the relaxed monoclinic crystal structure of NZSP$_{2.4}$ and Ta-substituted NZSP$_{2.4}$*

The monoclinic phase exhibits a similar vacancy-driven correlated migration mechanism as the rhombohedral structure. Ion conduction in the monoclinic phase is shown in Supplementary **Fig. S11(a)**, where Ta^{5+} substitution at the Zr^{4+} site generates Na vacancies and mid-Na sites anisotropic elongate along the c-direction, facilitating correlated Na^{+} migration (Supplementary **Fig. S11b**). Our calculations confirm this mechanism, and the corresponding volume changes for Ta-substituted and unsubstituted $NZSP_{2.4}$ are provided in Supplementary **Table S4**.

Table S4. *Unit cell parameters and volumes of* $NZSP_{2.4}$ *and Ta-*$NZSP_{2.4}$ *in the monoclinic phase extracted from simulated results.*

Composition	a (Å)	b (Å)	c (Å)	β	Volume(Å^3)
$NZSP_{2.4}$	16.00235	9.26898	9.24284	124.8672	1124.807
Ta -$NZSP_{2.4}$	15.85547	9.21114	9.33338	123.9130	1131.222

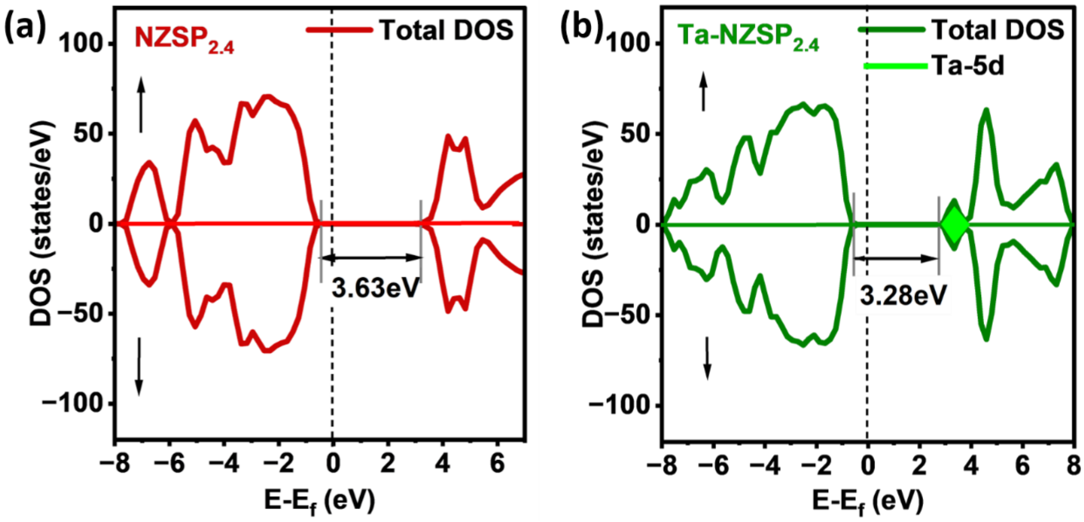

Figure S12. *The density of states of Monoclinic (a)* $NZSP_{2.4}$ *and (b) Ta-substituted* $NZSP_{2.4}$*.*

Similar to the rhombohedral structure, the band gap of monoclinic $NZSP_{2.4}$ (3.63 eV) decreases slightly to 3.28 eV upon Ta doping, as shown in **Fig. S12**. Likewise, the activation energy of monoclinic $NZSP_{2.4}$ is significantly reduced from 0.351 eV to 0.168 eV, as shown in **Fig. S13**, following the same mechanism observed for the rhombohedral structure, as discussed in Section 3.3 of the manuscript.

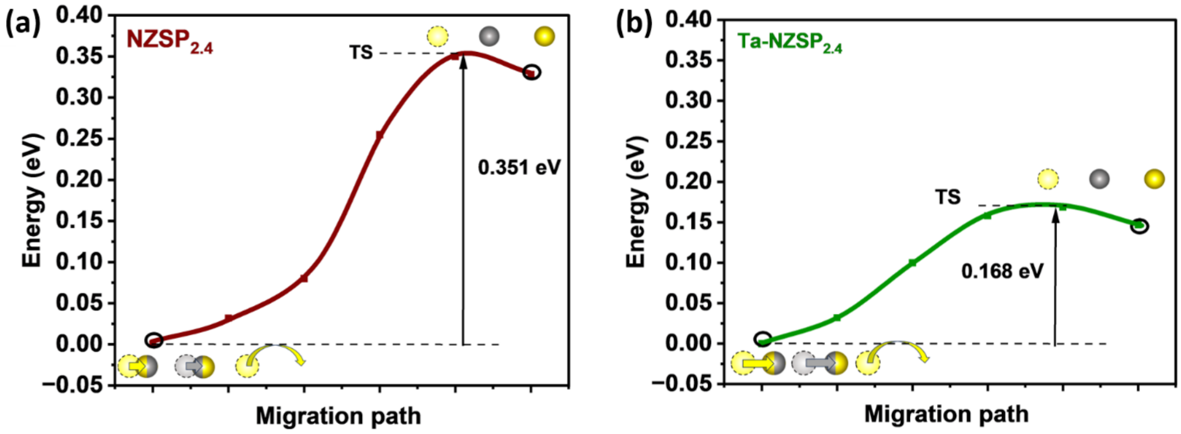

Figure S13. *NEB profiles for Monoclinic structure (a) NZSP$_{2.4}$ and (b) Ta-substituted NZSP$_{2.4}$*

.

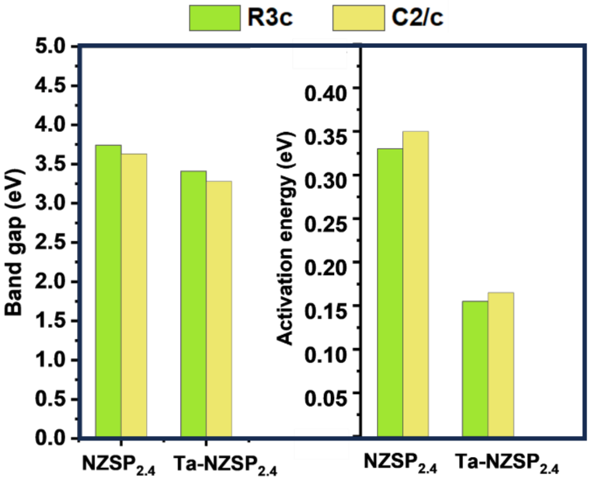

Figure S14. *Theoretical properties comparison of C2/c and R3c structure for NZSP$_{2.4}$ and Ta-substituted NZSP$_{2.4}$*

The calculated activation energies for rhombohedral and monoclinic NZSP$_{2.4}$ are 0.33 eV and 0.35 eV, respectively, indicating only a small difference in their ionic conduction properties.

The theoretical minimum activation energies are 0.168 eV for monoclinic Ta–$NZSP_{2.4}$ and 0.155 eV for rhombohedral Ta–$NZSP_{2.4}$, suggesting that their ionic conductivities are also comparable. Similarly, the band gap values are comparable in both phases, indicating no significant difference in their electronic properties. Although the rhombohedral phase shows slightly better performance, the difference in ionic properties between the two phases is not substantial enough to impact the overall behaviour of the mixed phase.

References

1 Z. Zhang, Z. Zou, K. Kaup, R. Xiao, S. Shi, M. Avdeev, Y. S. Hu, D. Wang, B. He, H. Li, X. Huang, L. F. Nazar and L. Chen, *Adv Energy Mater*, 2019, 9, 2001486.

2 L. Ran, A. Baktash, M. Li, Y. Yin, B. Demir, T. Lin, M. Li, M. Rana, I. Gentle, L. Wang, D. J. Searles and R. Knibbe, *Energy Storage Mater*, 2021, 40, 282–291.

3 J. Wang, T. He, X. Yang, Z. Cai, Y. Wang, V. Lacivita, H. Kim, B. Ouyang and G. Ceder, *Nat Commun*, 2023, 14, 5210.

4 Z. Zhang, S. Wenzel, Y. Zhu, J. Sann, L. Shen, J. Yang, X. Yao, Y. S. Hu, C. Wolverton, H. Li, L. Chen and J. Janek, *ACS Appl Energy Mater*, 2020, 3, 7427–7437.

5 Q. Ma, C. L. Tsai, X. K. Wei, M. Heggen, F. Tietz and J. T. S. Irvine, *J Mater Chem A*, 2019, 7, 7766–7776.

6 J. Xu, H. Tao, Z. Deng, X. Yang and L. Z. Fan, *J Materiomics*, 2024, 10, 1243–1251.

7 A. Chakraborty, R. Thirupathi, S. Bhattacharyya, K. Singh and S. Omar, *J Power Sources*, DOI:10.1016/j.jpowsour.2023.233092.

8 R. J. Miao, X. G. Cao, W. G. Wang and H. Y. Zhang, *Ceram Int*, 2021, 47, 17455–17462.

9 Y. Liu, L. Liu, J. Peng, X. Zhou, D. Liang, L. Zhao, J. Su, B. Zhang, S. Li, N. Zhang, Q. Ma and F. Tietz, *J Power Sources*, DOI:10.1016/j.jpowsour.2021.230765.

10 M. Akbar, I. Moeez, Y. H. Kim, M. Kim, J. Jeong, E. Lee, A. H. U. Bhatti, J. H. Park and K. Y. Chung, *Carbon Energy*, DOI:10.1002/cey2.717.

11 X. Wang, J. Chen, Z. Mao and D. Wang, *Chemical Engineering Journal*, DOI:10.1016/j.cej.2021.130899.

12 S. Yang, J. Liang, J. He, D. Fang, Y. Zhao, Y. Ding, A. Yin, Y. Li, C. Wang, J. Li and H. Jin, *ACS Appl Energy Mater*, 2024, 7, 9863–9871.

13 M. Akbar, I. Moeez, A. H. Umar Bhatti, Y. H. Kim, M. Kim, J. Y. Kim, J. Jeong, J. H. Park and K. Y. Chung, *Chem Eng J*, DOI:10.1016/j.cej.2025.164300.

14 J. He, S. Yang, X. Xiao, D. Fang, R. Miao, C. Wang, L. Chen, N. Li, J. Li, Y. Su and H. Jin, *Energy Storage Mater*, DOI:10.1016/j.ensm.2025.104037.

15 Z. Li, M. Zhang, Y. Yan, W. Zhang, X. Meng and N. Yang, *EES Batteries*, DOI:10.1039/d5eb00075k.

16 D. Li, C. Sun, C. Wang, J. Li, Z. Wang and H. Jin, *Energy Storage Mater*, 2023, 54, 403–409.

17 Y. Li, Z. Wang, C. Sun, S. Liu, Y. Dou, X. Yuan, H. Jin and Y. Zhao, *Adv Funct Mater*, DOI:10.1002/adfm.202425995.

18 Y. Li, C. Sun, Z. Sun, M. Li, H. Jin and Y. Zhao, *Adv Funct Mater*, DOI:10.1002/adfm.202403937.